Hidden variable in the electrocaloric effect of ferroics

Ravi Kashikar[§],[1,*] Subhashree Chatterjee[§],[2] Folarin Shola Taofeek,[1] Abhisikta Barman,[2] Shubhankar Barman,[3] Sohini Kar-Narayan,[4] Anuja Datta,[3] Sergey Lisenkov,[1] Devajyoti Mukherjee,[2,†] and I. Ponomareva[1,‡]

[1]*Department of Physics, University of South Florida, Tampa, Florida 33620, USA*

[2]*School of Physical Sciences, Indian Association for the Cultivation of Science, 2A & 2B Raja S. C. Mullick Road, Kolkata 700032, India*[§]

[3]*School of Applied and Interdisciplinary Sciences, Indian Association for the Cultivation of Science, 2A & 2B Raja S. C. Mullick Road, Kolkata 700032, India*

[4]*Department of Materials Science & Metallurgy, University of Cambridge, 27 Charles Babbage Road, Cambridge CB3 0FS, United Kingdom*

(Dated: December 13, 2022)

Abstract

Caloric effects allow for temperature control through adiabatic application of external fields and are actively explored for solid state refrigeration. The common wisdom is that the application of ultrahigh fields enhances the effects, thus providing a route to their practical applications. Using the ferroelectric relaxor (Ba, Ca)(Ti, Zr)O_3, we demonstrate that in ferroics, which are the prime candidates for such application, this is not true in general, and that caloric effects can be enhanced through the reduction of the applied field. The explanation of such a counterintuitive response is in the dependence of the electrocaloric effect on the effective poling field that can be regarded as a "hidden" variable of the caloric effects.

I. INTRODUCTION

Caloric effects are under active investigation owing to the groundbreaking findings of giant caloric effects in ferroics[1–12] and their promise for solid state coolers that are energetically efficient and environmentally friendly alternatives to conventional refrigeration[13,14]. The effect is defined as the reversible change in temperature under adiabatic application of electric, magnetic or stress fields. For example, the electrocaloric effect is associated with a reversible change in temperature under adiabatic application of electric field and can be quantified with the help of thermodynamics, in particular, Maxwell's equation:

$$\Delta T \approx -\frac{T}{\rho C_E}\int_{E_1}^{E_2}\left(\frac{\partial P}{\partial T}\right)_E dE. \tag{1}$$

where, P, T, and C_E are polarization, temperature and specific heat at constant electric field, respectively, while E, and ρ are the electric field and materials density, E_1 and E_2 are the initial and final values of the applied electric field. Typically caloric effects are rather small (on the order of a Kelvin under applied fields of 10-40 kV/cm) for practical applications. However, Eq. (1) suggests that electrocaloric ΔT can be increased by the application of large electric fields E_2, which is only possible in high quality samples. Indeed, the groundbreaking approach of using ultrathin high-quality films to achieve giant electrocaloric effect through application of high electric fields[1] has promoted an unprecedented research interest in electrocaloric effects with the number of publications increasing exponentially in the last decade[7]. More precisely, in Ref.[1] application of electric field of up to 776 kV/cm to poled antiferroelectric Pb(Ti, Zr)O_3 films was predicted to yield 12 K change in temperature[1]. The followup studies reported that in multilayer thick film of ferroelectric $BaTiO_3$ application of 800 kV/cm resulted in 7.1 K change in temperature[15]. $Ba_{0.8}Sr_{0.2}TiO_3$ films exhibited electrocaloric ΔT of 9.1 K under the field of 1000 kV/cm[16], while $BaZr_{0.2}Ti_{0.8}O_3$[17] thin films were reported to produce 43.6 K temperature change under electric field of 1011 kV/cm. Furthermore, in polymer/$Ba_{0.67}Sr_{0.33}TiO_3$ nanocomposites the field of 1500 kV/cm yielded 32 K change in temperature[18]. Although the field of electrocaloric measurements is often faulted by the reproducibility issues, still inspection of over 36 studies compiled in Ref.[7] suggests that the general trend is in agreement with expectation from Eq. (1), that is larger fields lead to larger electrocaloric ΔT. This can be further illustrated in the case of ferroelectric polymers where nearly linear increase in ΔT with electric field was reported[18].

Here, we grew a high quality epitaxial thin film of ferroelectric $(Ba_{0.85}Ca_{0.15})(Ti_{0.9}Zr_{0.1})O_3$ (BCZT) which allowed for the application of ultra high electric fields up to 1000 kV/cm. Surprisingly, we found that (i) such films remain in the ferroelectric phase up to 140 K above the Curie point (T_C = 360 K) of their bulk counterpart; (ii) the application of ultra high electric fields suppresses the electrocaloric effect. With the help of first-principles-based simulations we reveal that there exists a "hidden" variable in the caloric effects of ferroics that is responsible for the aforementioned findings and which can be manipulated to tune electrocaloric effect in a very counterintuitive way. For example, we demonstrate that in a given temperature range the largest electrocaloric change in temperatures is enhanced by a factor of seven through a two times *decrease* of the electric field.

II. METHODS

A dense ceramic target of $(Ba_{0.85}Ca_{0.15})(Ti_{0.9}Zr_{0.1})O_3$ (BCZT) was prepared by a conventional solid state reaction starting from high purity (99.99%) powders. The details of the bulk BCZT ceramic preparation is provided in the Supplemental Material. The as-prepared $(Ba_{0.85}Ca_{0.15})(Ti_{0.9}Zr_{0.1})O_3$ bulk ceramic was characterized for phase purity, structural refinement and chemical composition using X-ray diffraction (XRD), energy dispersive spectroscopy (EDS), x-ray photoelectron spectroscopy (XPS) and Raman spectroscopy (see Figures S1 in the Supplemental Material). Temperature dependent dielectric and ferroelectric measurements of the bulk pellet were conducted with a planar capacitor structure using sputtered Au top and bottom electrodes (see Figure S2 in the Supplemental Material).

An epitaxial $(Ba_{0.85}Ca_{0.15})(Ti_{0.9}Zr_{0.1})O_3$ thin film heterostructure using $La_{0.7}Sr_{0.3}MnO_3$ (LSMO) top and bottom electrodes was fabricated on a single-crystal $SrTiO_3$ (STO) (100) substrate using a commercial pulsed laser deposition (PLD) system. The details of the thin film fabrication and characterization is provided in the Supplemental Material. The crystallinity, strain, composition, surface morphology and interfacial micro-structures of the BCZT/LSMO heterostructure were investigated using symmetric/asymmetric XRD, EDS, XPS, atomic force microscopy (AFM) and high-resolution transmission electron microscopy (HRTEM) (see Figure S3 and S4 in the Supplemental Material). Temperature dependent dielectric measurements of the LSMO/BCZT/LSMO thin film capacitor were conducted in the frequency range of 1 kHz to 1 MHz by using a precision digital LCR meter (see Figure

S5 in the Supplemental Material). Temperature dependent ferroelectric hysteresis loops for the BCZT thin film were measured using a commercial ferroelectric test system (Radiant Technologies Inc.) equipped with a micro-probe station at a frequency of 1 kHz in different ranges of electric fields from [-400:400] kV/cm to [-1000:1000] kV/cm.

Computationally, we model bulk $Ba(Ti_{1-x},Zr_x)O_3$ using first-principles-based effective Hamiltonian of Ref.[19]. We chose $Ba(Ti_{0.9},Zr_{0.1})O_3$ as the closest material to (Ba, Ca)(Ti, Zr)O_3 for which reliable computational approach is available. The degrees of freedom for the Hamiltonian include local soft modes which are proportional to the local dipole moments and local strain variables that describe deformation of the unit cells. The Hamiltonian includes the interactions that are responsible for the ferroelectricity in $Ba(Ti_{1-x},Zr_x)O_3$: local mode self energy up to fourth order, harmonic short and long range interactions between the local modes, elastic deformations and interactions responsible for the electrostriction, and the term that describes interaction of local modes with the electric field. The Hamiltonian reproduces correctly complex phase diagram of temperature vs Zr concentration in $BaTiO_3$[19]. Note, that $Ba(Ti_{1-x},Zr_x)O_3$ bulk is simulated by applying periodic boundary conditions along all three Cartesian directions. To model hysteresis loops the effective Hamiltonian is used in the framework of classical molecular dynamics (MD) with Evans-Hoover thermostat[20] to simulate NPT ensemble. The integration step is 1 fs. The ac electric field is simulated with the amplitudes of 50, 500, and 5000 kV/cm and frequency 0.01 THz. Technically, three periods of the field are simulated and the data are then averaged. The simulation supercell size is $30 \times 30 \times 30$ unit cells of perovskite. The hysteresis loops are simulated for the temperature interval from 300 K to 510 K in steps of 10 K.

To compute electrocaloric change in temperature we integrate numerically Eq. (1). For that hysteresis loops $P(E)$ in the first quadrant are used to compute $P(T, E)$ dependencies. Technically, for a given E we first fit $P(T)$ dependencies and then compute analytical derivative $\left(\frac{\partial P}{\partial T}\right)_E$, which are then used to integrate Eq. 1 numerically using Simpson's method as implemented in SciPy module[21]. We found that fitting of $(\frac{\partial P}{\partial T})_E$ has a crucial role and can introduce spurious peaks and lead to incorrect predictions for ΔT. One way to avoid the artifacts is to compare the predictions from the fitted data with those of unfitted data, that is when the aforementioned derivative is computed numerically. We empirically found that sometimes fitting with the nth order polynomial works well, while sometimes we have to use spline fitting[21]. In all cases the reported data have been properly validated by comparison

with numerical derivative approach. We have used experimental value for heat capacity $C =$ 540 J/Kg-K[22].

To simulate electrocaloric effect directly we used both adiabatic and isothermal simulations. The adiabatic simulations were carried out using our original semi-classical approach, that is the isentropic Monte Carlo that incorporates quantum mechanical effect into the heat capacity[23]. The simulation supercell cell was $16 \times 16 \times 16$. We first simulate hysteresis loops using Metropolis Monte Carlo and then use zero field structures to initialize direct adiabatic simulations. In the latter simulations the electric field was slowly increased from 0 to E_0 kV/cm and then decreased back to zero at a rate of E_0/N_{MC} kV/cm per one Monte Carlo sweep. Here $N_{MC} = 100000$ is the number of MC sweeps used for the field application. This cycle of field application has been repeated twice so that the electrocaloric change in temperature can be investigated in the second cycle, after the simulated sample already experienced the field E_0. For the isothermal simulations we used MD with the supercell of $30 \times 30 \times 30$ following the computational approach of Ref.[24]. Note, that the difference between the supercell size between the two simulations is due to the difference in the computational efficiency of MD and Monte Carlo simulations (with the former one being much faster). In this simulations we simulate *ac* electric field with amplitudes in the range 50 to 10,000 kV/cm and frequency of 0.5 GHz. The computations allow to harvest isothermal heat which can then be converted into adiabatic temperature change $\Delta T = Q/C$. We focus only on the reversible parts of the simulations.

III. RESULTS AND DISCUSSION

We begin with electrocaloric effect in bulk $(Ba_{0.85}Ca_{0.15})(Ti_{0.9}Zr_{0.1})O_3$ ceramics. Figure 1(a) shows the ferroelectric hysteresis loops obtained at different temperatures. The largest field that we were able to apply to the sample was 34 kV/cm. The hysteresis loops data were used to get the dependencies of the electric polarization on temperature for different electric field [see Fig. 1(b)], which are then employed in the framework of the indirect approach of Eq. (1) to estimate the electrocaloric change in temperature as detailed in Section II. For this study we use E_1 =0 kV/cm and $E_2 = \Delta E$. The electrocaloric change in temperature is given in Fig. 1(c). The peak in ΔT occurs at 363 K which is near the location of maximum in the temperature dependence of the dielectric constant (see Fig. S2 in the

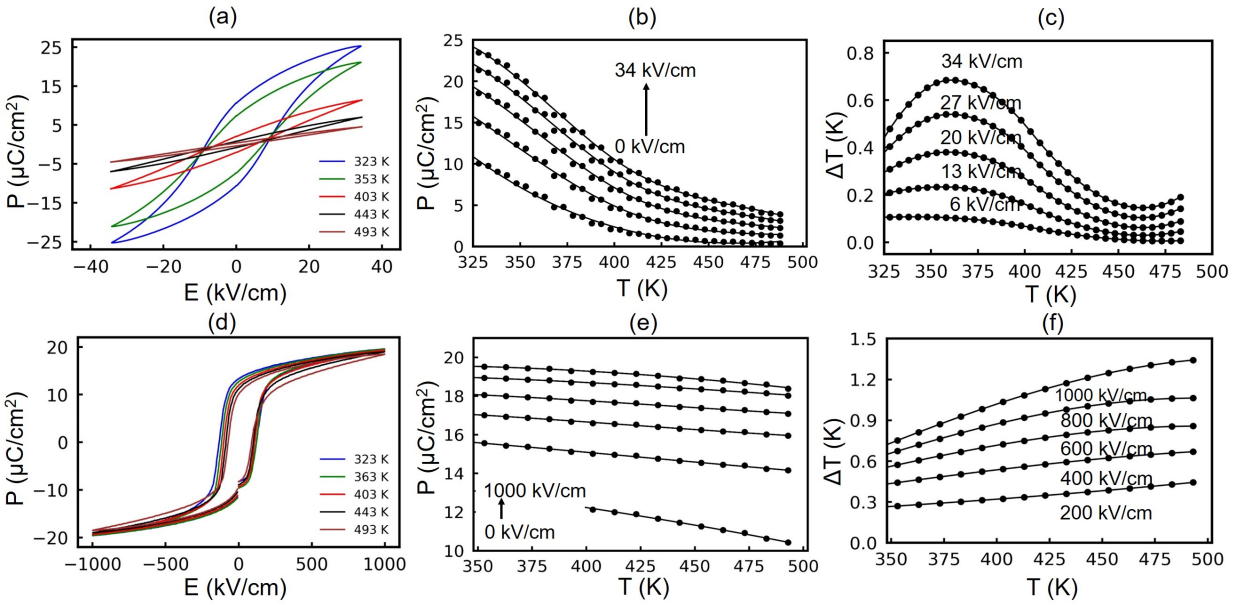

FIG. 1. Polarization as a function of applied electric field (a), temperature (b); and electrocaloric change in temperature as a function of temperature in bulk BCZT (c). Panels (d)-(f) present same dependencies but for 100 nm thick BCZT film.

Supplemental Material). The latter maximum is at 360 K and typically associated with the Curie point. So, we conclude that under the conditions of measurements the maximum electrocaloric ΔT occurs in close vicinity of the Curie point. For the chosen experimental conditions the largest electrocaloric change in temperature is 0.75 K at 363 K under ΔE of 34 kV/cm, which agrees with previous reports on bulk ceramics[25,26]. The common wisdom rooted in Eq. (1) is that ΔT can be increased through application of high fields, which, in turn, could be achieved in high quality thin films[1]. For this study, an epitaxial $(Ba_{0.85}Ca_{0.15})(Ti_{0.9}Zr_{0.1})O_3$ thin film heterostructure using $La_{0.7}Sr_{0.3}MnO_3$ top and bottom electrodes was fabricated on a single-crystal $SrTiO_3$ (100) substrate using a commercial pulsed laser deposition system[27]. Details on the films growth and characterization can be found in the Supplementary Material (See Figs. S3 and S4). The high-quality epitaxial BCZT thin film grown using PLD lead to high values of the dielectric constant (see Fig. S5 in the Supplemental Material) which allowed for the application of ultra high fields up to 1000 kV/cm, that is 30 times increase with respect to the bulk. The associated hysteresis loops are given in Fig. 1(d) and reveal a striking feature: the films remain in the ferroelectric phase in the entire temperature range, that is much above the Curie point of 363 K. As

before the data were used within the indirect approach of Eq. (1) to estimate electrocaloric ΔT [see Fig. 1(f)]. Surprisingly, the data reveal that despite nearly 30 times increase in the applied electric field the maximum ΔT has only increased 2 times. This is a very discouraging finding as thin films are prime candidates for practical application, exactly for the reason of allowing higher fields applications. Does our finding suggest that thin-film route may not bring the desired breakthrough for the solid-state cooling?

To gain an insight into such an unexpected finding we turn to first-principles-based simulations and focus on the role that the electric field plays in the effect. The advantage of simulations is that they can assess the range of fields beyond those accessible in experiment. Figure 2 gives simulated hysteresis loops in bulk $Ba(Ti_{0.9},Zr_{0.1})O_3$ for different range of applied electric field, $[-E_0 : E_0]$. The data predict that the change of E_0 has a dramatic effect on the hysteresis loops. Most importantly, for the largest field range the simulated supercell exhibits ferroelectric behavior in the entire temperature range investigated, that is beyond the computational Curie point of 410 K for the material[19]. This reproduces the unusual experimental finding reported in Fig. 1(d) and suggests that the application of ultra high fields could stabilize the ferroelectric phase beyond the Curie point, the effect that we term as "superpoling" of ferroelectric. We hypothesize that superpoling of a ferroelectric is similar to supercooling/superheating of liquid. Such regimes are associated with a transient existence (sometimes brief, sometimes long) of a metastable phase at the temperatures at which the chemical potential of the stable phase is lower[28]. In analogy, the superpoled state of a ferroelectric is a metastable polar phase **of transient existence** that persists at zero field and above the material's Curie point. For first order phase transitions in the vicinity of the Curie point the free energy has minima at $P = 0$ and $P \neq 0$ values of the order parameter[29], [see inset in the Fig. 2(c)]. The metastable superpoled state is associated with $P \neq 0$ local minima. To test our hypothesis we compute the zero field dipoles distributions at 520 K (that is 110 K above the computational Curie point) from the simulations with $E_0 = 50$ and 5000 kV/cm. The plots are given in the inset to Fig. 2(c). For $E_0 = 50$ kV/cm the dipoles distribution is symmetric and centered at $P = 0$, the microstate corresponds to $P = 0$ global minimum of free energy. For $E_0 = 5000$ kV/cm the distribution is slightly asymmetric and centered at finite value of polarization, the microstate corresponds to $P \neq 0$ local minimum of the free energy. These confirm that the superpoled state is the metastable state of the system. Such transient states are more likely to appear in high purity samples or in simula-

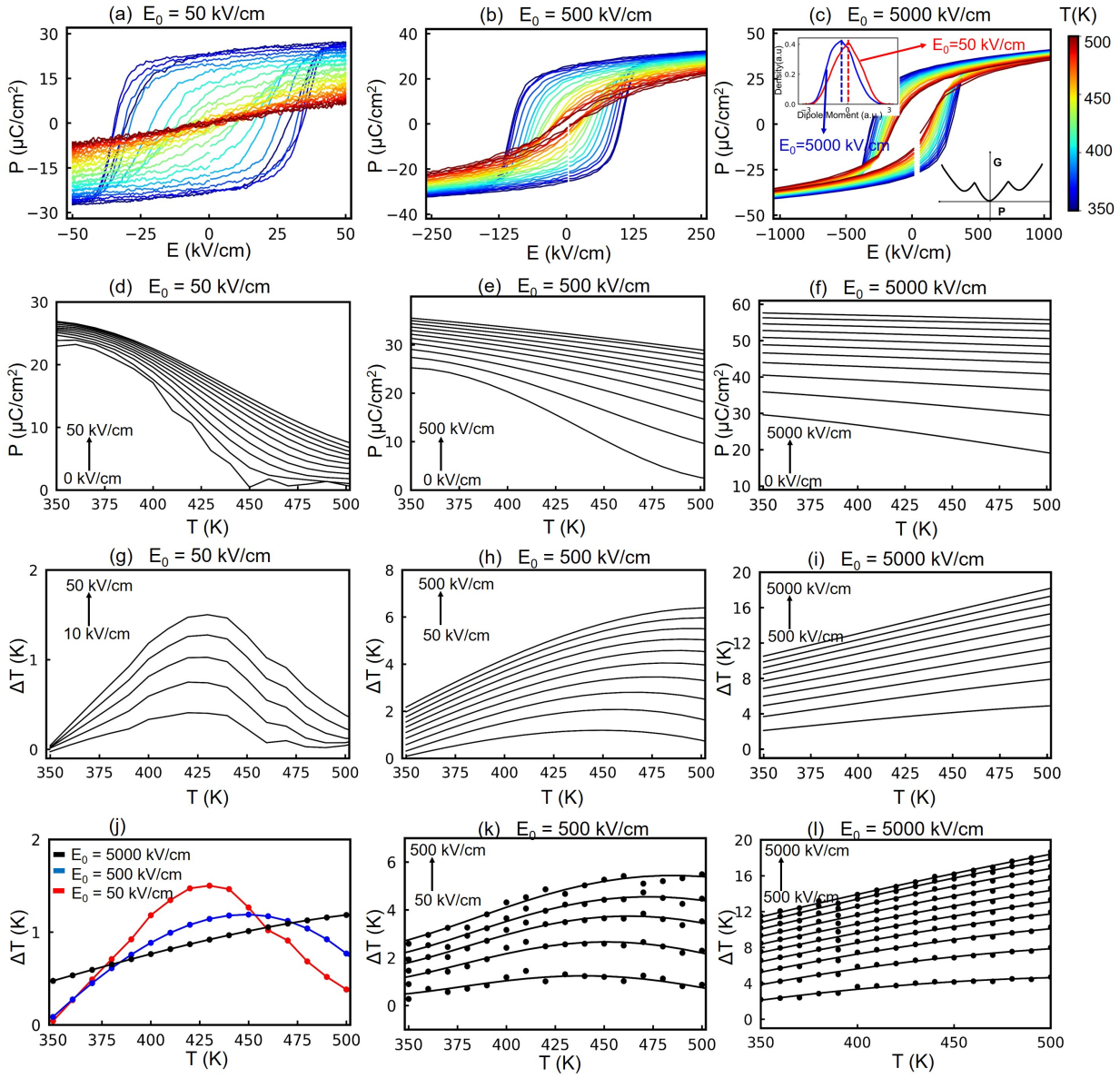

FIG. 2. Ferroelectric hysteresis loops obtained in MD simulations with different range of electric fields: [-50:50] kV/cm (a), [-500:500] kV/cm (b) ; and [-5000:5000] kV/cm (c). In (c) left inset gives zero field dipoles distribution function at 520 K for two different values of the poling field. Right inset is schemtic free energy landscape in the vicinity of first order phase tansition. Dependence of polarization on temperatures (d)-(f) obtained from the data of panels (a)-(c), respectively. Electrocaloric change in temperature (g)-(i) computed from dependencies of panels (d)-(f) using Eq. (1). Electrocaloric change in temperature as a function of temperature due to application of 50 kV/cm field (j). Different curves correspond to different values of the poling field as given in the legend. Electrocaloric $\Delta T(T)$ obtained from direct adiabatic simulations for different value of E_0 as given in the titles (k)-(l).

tions, which lack nucleation sites. Note that the slight asymmetry in E_0 =5000 kV/cm data is due to small population of dipoles in the $P = 0$ minimum of free energy.

Superpoling also affects coercive field as evident from Figs. 2(a)-(c). In all cases we find the same nucleation-limited-switching[30], which is mostly homogeneous nucleation of extremely small domains of opposite polarization, followed by their growth and coalescence. Distribution functions for dipole moments computed during polarization reversal reveal that supercell passes through $P = 0$ phase similar to the one shown in Fig. 2(c) inset. Since superpoling **temporarily** "traps" the system in $P \neq 0$ phase larger fields are needed to get to $P = 0$ phase, which explains higher coercive fields in the superpoled state.

It is convenient to term the largest in magnitude field that the sample experiences (either in the *ac* or *dc* regime), E_0, as the effective poling field. The strong dependence of the polarization response on this effective poling field necessitates to add E_0 as an additional variable for the polarization. In other words, the polarization is now a function of temperature, applied electric field, and the effective poling field, that is $P(E, T, E_0)$. Interestingly, this finding suggests that for such materials Eq. (1) should be written as $\Delta T \approx -\frac{T}{\rho C_E}\int_{E_1}^{E_2}(\frac{\partial P}{\partial T})_{E,E_0}dE$, which reveals that the electrocaloric ΔT is a function of the effective poling field, that is $\Delta T(T, E_0, E_1, E_2)$. Integration of this expression for the $P(E, T, E_0)$ dependencies harvested in computations [see Figs. 2(a)-(f)] give electrocaloric $\Delta T(T, E_0, \Delta E)$ shown in Figs. 2(g)-(i). The data reveal drastic change in the shape of curves as poling field increases. The most striking feature is the dramatic shift in the position of the peak in $\Delta T(T)$. As applied electric field increases the peak shifts toward higher temperatures and finally moves outside of the simulated temperature range [see Fig. 2(i)]. This is exactly what happens as experimentally we switch from bulk (low E_0 =34.4 kV/cm) to high quality thin films (high E_0 =1000 kV/cm). The peak moves outside the measured range, which explains unexpectedly low values of ΔT inside the range. An explicit demonstration of the dependence of ΔT on E_0 can be achieved through keeping ΔE constant as it is done in Fig. 2(j), where the shift in the position of ΔT_{max} as E_0 increases is very clear. The shift in the position of ΔT_{max} towards higher temperature has been reported in Ref.[5] where it was found that a line of maximum electrocaloric effect passes through the zero field ferroelectric transition, continuing along a Widom line at high temperatures with increasing fields. Our data in Figs. 2(d)-(f) demonstrate that such zero field ferroelectric transition is a function of the poling field, which explains the shift in the position of ΔT_{max} as a function of E_0 for low

ΔE (Figs. 2(g)-(i)).

After these demonstrations one may wonder if the role of the hidden variable E_0 is enhanced (or even introduced in the first place) by the application of the indirect approach of Eq. (1). To answer this question we carried out direct simulations of electrocaloric effect using both adiabatic semi-classical Monte Carlo (MC)[23] and isothermal MD[24] approaches as detailed in Section II. Data from direct adiabatic simulations are presented in Figs. 2(k)-(l) and demonstrate good agreement with predictions from indirect approach. Data from direct isothermal simulations are given in the Supplemental Material (see Fig. S6) and are in agreement with both indirect predictions and direct adiabatic simulations. Consequently, direct simulations confirm the trends found in the indirect predictions. In particular, we find dependence on the effective poling field in both types of direct simulations and conclude that the effects reported here are not introduced by the application of the indirect methodology. We would also like to note, that we have previously demonstrated that direct and indirect approaches provide identical results if the data from the same branch of hysteresis loop are used and the irreversible regions around the coercive field are excluded[31]. All of our indirect data are within the region of the indirect approach validity.

Having achieved the understanding of the role that poling plays in the electrocaloric ΔT we now aim to manipulate E_0 in order to enhance the electrocaloric effects in our films. Figure 2 suggests that it should be possible to shift the position of the peak in ΔT to lower temperatures by reducing the effective poling field and avoiding superpoling. We repeated our experiment on the same film but with reduced electric field of 500 kV/cm. The data are given in Fig. 3 and demonstrate that, indeed, reducing the electric field brings the position of ΔT_{max} within the temperature range of the measurements (and close to the Curie temperature of bulk). This results in a 7 times enhancement of largest ΔT value in the given temperature range as compared to the high field data. This finding not only demonstrates the possibility to manipulate electrocaloric effect by the effective poling field but also reveals a counterintuitive enhancement of the electrocaloric effect through the reduction of electric field. The value of ΔT_{max} =8.5 K is in the range of computational predictions from direct adiabatic approach of 5.4 to 7.2 K for applied fields of 500 to 800 kV/cm which are below the superpoling regime in computations (Fig. S7 in the Supplementary Material). Figure 3(d) shows the dependence of the largest ΔT on the applied field (the case of $E_0 = \Delta E$) from the hysteresis loops measured on the film (see also Fig. S8 of Supplemental Material). Below

500 kV/cm ΔT_{max} increases with field. Above this value we find that largest ΔT decreases as a function of field as superpoled regime sets at 1000 kV/cm. The position of the peak in $\Delta T(T)$ reported in the same figure shifts towards higher temperature for all fields.

We note that our experimental thin films are under small compressive strain of -0.15% (see Supplementary Material) , which may further contribute to the stabilization of ferroelectric phase above bulk T_C[32–34] and associated decrease in ΔT. For example, we found out in computations under compressive strain of -0.22% strain with respect to cubic lattice constant that the Curie temperature increases by 30 K causing the peak in $\Delta T(T)$ to shift towards higher temperatures. Comparison between ΔT_{max} for the same E_0 and ΔE for the unstrained and strained supercells reveals a slight enhancement due to compressive strain (see Fig. S9 of the Supplemental Material). Nevertheless, strain by itself cannot account for our main findings. Indeed, the measurements carried out on the same film under different fields [see Fig. 1(d) and Fig. 3(a)] fix the strain, while demonstrate significant dependence of both hysteresis loops and electrocaloric ΔT on the poling field.

One may wonder if the effects reported here are common for ferroelectrics or just specific for the material we considered. To gain some insight we repeated simulations for $BaTiO_3$, which is a prototypical ferroelectric. Surprisingly, we found the aforementioned dependencies on E_0 to hold even in this material (see Fig. S10 in the Supplemental Material), which provides an evidence that they are likely to be common to ferroelectrics. Of course, some ferroelectrics could have only weak dependence on E_0, while others could have a strong one, like the one we considered in this study.

IV. CONCLUSIONS

In summary, we have reported that electrocaloric effect in ferroics exhibits a strong and counterintuitive dependence on the effective poling field, which can be viewed as a "hidden" variable of the caloric effect. This hidden variable becomes extremely powerful at the nanoscale, where fields could reach thousands of kV/cm, and could lead to "superpoling" of thin films. Once superpoled the films exhibit ferroelectric behavior much above the materials Curie point which causes deterioration of the caloric response. On the positive side, this uncovered dependence on the effective poling field is an additional "knob" for the electrocaloric effect, which could be used for its enhancement. For example, we demonstrated that two

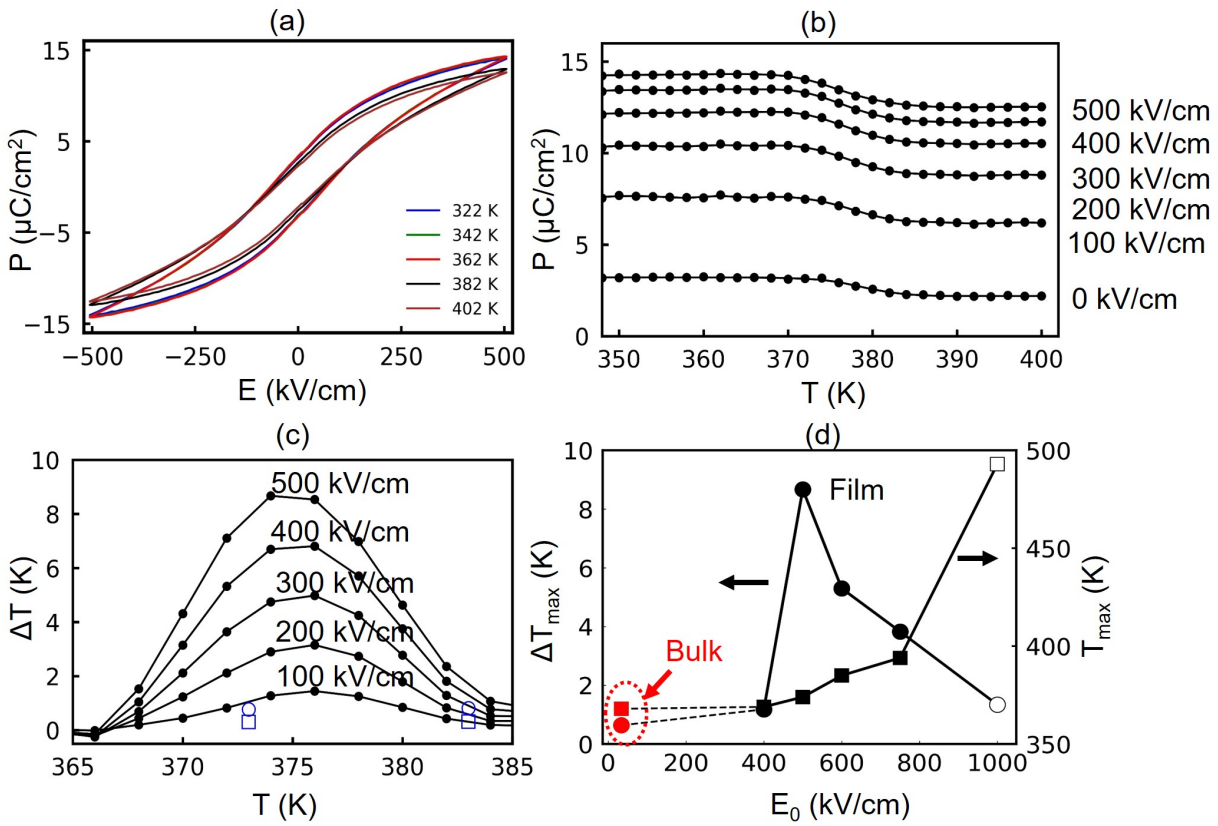

FIG. 3. Hysteresis loops (a) and associated temperature dependence of polarization (b) in 100 nm BCZT thin film for poling field of 500 kV/cm. Electrocaloric ΔT computed from experimental data using the approach of Eq. (1) (c). For comparison we include data for E_0 =1000 kV/cm and ΔE = 100 kV/cm (blue squares) and 500 kV/cm (blue circles). The peak electrocaloric temperature ΔT_{max} and its position T_{max} as a function of the poling field for the case $E_0 = \Delta E$ for both bulk ceramics and thin film (d). Open symbols correspond to the largest values in the given temperature range when the peak is outside the range.

times reduction of electric field results in seven times enhancement of the electrocaloric effect. As ferroics in general exhibit similar properties we expect that our findings would apply to this class in general and, therefore, are likely to bring new light into the entire family of caloric effects: magnetocaloric, barocaloric, multicaloric, and others, in addition to the electrocaloric effects considered here.

ACKNOWLEDGEMENTS

The computational work is supported by the U.S. Department of Energy, Office of Basic Energy Sciences, Division of Materials Sciences and Engineering under grant DE-SC0005245. D.M. acknowledges funding from the Technical Research Center, Department of Science and Technology, Government of India (Grant No. AI/1/62/IACS/2015) and Science and Engineering Research Board (SERB) Starting Research Grant, Government of India (Grant No. SRG/2019/000387). We acknowledge Prof. Suhrit Ghosh for giving permission to use the ferroelectric test system. A.D. acknowledges funding from SERB-Ramanujan Fellowship (Award No. SB/S2/RJN-057/2017) and SERB-Core Research Grant (Grant No: CRG/2020/002395). S.K.-N. acknowledges funding from a European Research Council Starting Grant (Grant No. ERC-2014-STG-639526, NANOGEN). S.C. acknowledges fellowship from DST-INSPIRE, Govt. of India. A.B. acknowledges fellowship from UGC-CSIR, Govt. of India. S.B. acknowledges CSIR-NET Fellowship, Govt. of India.

---

* ravik@usf.edu

† sspdm@iacs.res.in

‡ iponomar@usf.edu

§ These authors contributed equally to the work

[1] A. S. Mischenko, Q. Zhang, J. F. Scott, R. W. Whatmore, and N. D. Mathur. Giant Electrocaloric Effect in Thin-Film $PbZr_{0.95}Ti_{0.05}O_3$. *Science*, 311(5765):1270–1271, 2006. doi:10.1126/science.1123811. URL https://www.science.org/doi/abs/10.1126/science.1123811.

[2] A. S. Mischenko, Q. Zhang, R. W. Whatmore, J. F. Scott, and N. D. Mathur. Giant electrocaloric effect in the thin film relaxor ferroelectric $0.9PbMg_{1/3}Nb_{2/3}O_3$-$0.1PbTiO_3$ near room temperature. *Applied Physics Letters*, 89(24):242912, 2006. doi:10.1063/1.2405889. URL https://doi.org/10.1063/1.2405889.

[3] Yang Bai, Guangping Zheng, and Sanqiang Shi. Direct measurement of giant electrocaloric effect in $BaTiO_3$ multilayer thick film structure beyond theoretical prediction. *Applied Physics Letters*, 96(19):192902, 2010. doi:10.1063/1.3430045. URL https://doi.org/10.1063/1.3430045.

[4] Biaolin Peng, Huiqing Fan, and Qi Zhang. A Giant Electrocaloric Effect in Nanoscale Antiferroelectric and Ferroelectric Phases Coexisting in a Relaxor $Pb_{0.8}Ba_{0.2}ZrO_3$ Thin Film at Room Temperature. *Advanced Functional Materials*, 23(23):2987–2992, 2013. doi: https://doi.org/10.1002/adfm.201202525. URL https://onlinelibrary.wiley.com/doi/abs/10.1002/adfm.201202525.

[5] Maimon C. Rose and R. E. Cohen. Giant electrocaloric effect around T_c. *Phys. Rev. Lett.*, 109: 187604, Nov 2012. doi:10.1103/PhysRevLett.109.187604. URL https://link.aps.org/doi/10.1103/PhysRevLett.109.187604.

[6] Hui-Jian Ye, Xiao-Shi Qian, Dae-Yong Jeong, Shujun Zhang, Yue Zhou, Wen-Zhu Shao, Liang Zhen, and Q. M. Zhang. Giant electrocaloric effect in $BaZr_{0.2}Ti_{0.8}O_3$ thick film. *Applied Physics Letters*, 105(15):152908, 2014. doi:10.1063/1.4898599. URL https://doi.org/10.1063/1.4898599.

[7] Ajeet Kumar, Atul Thakre, Dae-Yong Jeong, and Jungho Ryu. Prospects and challenges of the electrocaloric phenomenon in ferroelectric ceramics. *J. Mater. Chem. C*, 7:6836–6859, 2019. doi:10.1039/C9TC01525F. URL http://dx.doi.org/10.1039/C9TC01525F.

[8] Jinglei Li, Yunfei Chang, Shuai Yang, Ye Tian, Qingyuan Hu, Yongyong Zhuang, Zhuo Xu, and Fei Li. Lead-free bilayer thick films with giant electrocaloric effect near room temperature. *ACS Applied Materials & Interfaces*, 11(26):23346–23352, 2019. doi:10.1021/acsami.9b06279. URL https://doi.org/10.1021/acsami.9b06279.

[9] Sagar E. Shirsath, Claudio Cazorla, Teng Lu, Le Zhang, Yee Yan Tay, Xiaojie Lou, Yun Liu, Sean Li, and Danyang Wang. Interface-charge induced giant electrocaloric effect in lead free ferroelectric thin-film bilayers. *Nano Letters*, 20(2):1262–1271, 2020. doi: 10.1021/acs.nanolett.9b04727. URL https://doi.org/10.1021/acs.nanolett.9b04727.

[10] Maofan Li, Shiguo Han, Yi Liu, Junhua Luo, Maochun Hong, and Zhihua Sun. Soft perovskite-type antiferroelectric with giant electrocaloric strength near room temperature. *Journal of the American Chemical Society*, 142(49):20744–20751, 2020. doi:10.1021/jacs.0c09601. URL https://doi.org/10.1021/jacs.0c09601.

[11] X. Moya and N. D. Mathur. Caloric materials for cooling and heating. *Science*, 370(6518): 797–803, 2020. doi:10.1126/science.abb0973.

[12] A. Torelló, P. Lheritier, T. Usui, Y. Nouchokgwe, M. Gérard, O. Bouton, S. Hirose, and E. Defay. Giant temperature span in electrocaloric regenerator. *Science*, 370(6512):125–129, 2020. doi:

10.1126/science.abb8045.

[13] Ichiro Takeuchi and Karl Sandeman. Solid-state cooling with caloric materials. *Physics Today*, 68(12):48–54, 2015. doi:10.1063/PT.3.3022. URL https://doi.org/10.1063/PT.3.3022.

[14] Abhisikta Barman, Sohini Kar-Narayan, and Devajyoti Mukherjee. Caloric effects in perovskite oxides. *Advanced Materials Interfaces*, 6(15):1900291, 2019. doi: https://doi.org/10.1002/admi.201900291. URL https://onlinelibrary.wiley.com/doi/abs/10.1002/admi.201900291.

[15] Yang Bai, Guang-Ping Zheng, Kai Ding, Lijie Qiao, San-Qiang Shi, and Dong Guo. The giant electrocaloric effect and high effective cooling power near room temperature for $BaTiO_3$ thick film. *Journal of Applied Physics*, 110(9):094103, 2011. doi:10.1063/1.3658251. URL https://doi.org/10.1063/1.3658251.

[16] Ran Su, Dawei Zhang, Yang Liu, Jiangbo Lu, Zhipeng Wang, Linglong Li, Jihong Bian, Ming Wu, Xiaojie Lou, and Yaodong Yang. Novel lead-free ferroelectric film by ultra-small $Ba_{0.8}Sr_{0.2}TiO_3$ nanocubes assembled for a large electrocaloric effect. *Phys. Chem. Chem. Phys.*, 18:29033–29040, 2016. doi:10.1039/C6CP05462E. URL http://dx.doi.org/10.1039/C6CP05462E.

[17] Fei Guo, Xin Wu, Qingshan Lu, and Shifeng Zhao. Near room temperature giant negative and positive electrocaloric effects coexisting in lead–free $BaZr_{0.2}Ti_{0.8}O_3$ relaxor ferroelectric films. *Ceramics International*, 44(3):2803–2808, 2018. ISSN 0272-8842. doi:https://doi.org/10.1016/j.ceramint.2017.11.022. URL https://www.sciencedirect.com/science/article/pii/S0272884217324641.

[18] Guangzu Zhang, Xiaoshan Zhang, Tiannan Yang, Qi Li, Long-Qing Chen, Shenglin Jiang, and Qing Wang. Colossal room-temperature electrocaloric effect in ferroelectric polymer nanocomposites using nanostructured barium strontium titanates. *ACS Nano*, 9(7):7164–7174, 2015. doi:10.1021/acsnano.5b03371. URL https://doi.org/10.1021/acsnano.5b03371. PMID: 26132841.

[19] C. Mentzer, S. Lisenkov, Z. G. Fthenakis, and I. Ponomareva. Phase evolution in the ferroelectric relaxor $Ba(Ti_{1-x}, Zr_x)O_3$ from atomistic simulations. *Phys. Rev. B*, 99:064111, Feb 2019. doi:10.1103/PhysRevB.99.064111. URL https://link.aps.org/doi/10.1103/PhysRevB.99.064111.

[20] D.C. Rapaport. *The Art of Molecular Dynamics Simulation*. Cambridge, 1997.

[21] Pauli Virtanen, Ralf Gommers, Travis E. Oliphant, Matt Haberland, Tyler Reddy, David Cournapeau, Evgeni Burovski, Pearu Peterson, Warren Weckesser, Jonathan Bright, Stéfan J. van der Walt, Matthew Brett, Joshua Wilson, K. Jarrod Millman, Nikolay Mayorov, Andrew R. J. Nelson, Eric Jones, Robert Kern, Eric Larson, C J Carey, İlhan Polat, Yu Feng, Eric W. Moore, Jake VanderPlas, Denis Laxalde, Josef Perktold, Robert Cimrman, Ian Henriksen, E. A. Quintero, Charles R. Harris, Anne M. Archibald, Antônio H. Ribeiro, Fabian Pedregosa, Paul van Mulbregt, and SciPy 1.0 Contributors. SciPy 1.0: Fundamental Algorithms for Scientific Computing in Python. *Nature Methods*, 17:261–272, 2020. doi:10.1038/s41592-019-0686-2.

[22] Donglin Liu, Qiang Li, and Qingfeng Yan. Electro-caloric effect in a bczt single crystal. *CrystEngComm*, 20:1597–1602, 2018. doi:10.1039/C7CE02040F. URL http://dx.doi.org/10.1039/C7CE02040F.

[23] P. Jouzdani, S. Cuozzo, S. Lisenkov, and I. Ponomareva. Enhancement of electrocaloric response through quantum effects. *Phys. Rev. B*, 96:214107, Dec 2017. doi:10.1103/PhysRevB.96.214107. URL https://link.aps.org/doi/10.1103/PhysRevB.96.214107.

[24] S. Lisenkov and I. Ponomareva. High-frequency intrinsic dynamics of the electrocaloric effect from direct atomistic simulations. *Phys. Rev. B*, 97:184104, May 2018. doi:10.1103/PhysRevB.97.184104. URL https://link.aps.org/doi/10.1103/PhysRevB.97.184104.

[25] Jinfei Wang, Tongqing Yang, Shengchen Chen, Gang Li, Qingfeng Zhang, and Xi Yao. Nonadiabatic direct measurement electrocaloric effect in lead-free Ba,Ca(Zr,Ti)O_3 ceramics. *Journal of Alloys and Compounds*, 550:561–563, 2013. ISSN 0925-8388. doi:https://doi.org/10.1016/j.jallcom.2012.10.144. URL https://www.sciencedirect.com/science/article/pii/S0925838812019238.

[26] Zouhair Hanani, Soukaina Merselmiz, Daoud Mezzane, M'barek Amjoud, Andraž Bradeško, Brigita Rožič, Mohammed Lahcini, Mimoun El Marssi, Andrey V. Ragulya, Igor A. Luk'yanchuk, Zdravko Kutnjak, and Mohamed Gouné. Thermally-stable high energy storage performances and large electrocaloric effect over a broad temperature span in lead-free bczt ceramic. *RSC Adv.*, 10:30746–30755, 2020. doi:10.1039/D0RA06116F. URL http://dx.doi.org/10.1039/D0RA06116F.

[27] Subhashree Chatterjee, Abhisikta Barman, Shubhankar Barman, Tanmay Chabri, Sohini Kar-Narayan, Anuja Datta, and Devajyoti Mukherjee. Role of oxygen vacancies on the low-

temperature dielectric relaxor behavior in epitaxial $Ba_{0.85}Ca_{0.15}Ti_{0.9}Zr_{0.1}O_3$ thin films. *Phys. Rev. Materials*, 5:064415, Jun 2021. doi:10.1103/PhysRevMaterials.5.064415. URL https://link.aps.org/doi/10.1103/PhysRevMaterials.5.064415.

[28] Charles Kittel. *Introduction to Solid State Physics*. John Wiley & Sons, Inc., New York, 6th edition, 1986.

[29] Karin M. Rabe, Karin M. Rabe, Charles H. Ahn, and Jean-Marc Triscone. *Physics of Ferroelectrics: A Modern Perspective*. Springer Publishing Company, Incorporated, 1st edition, 2007. ISBN 3540345906.

[30] Alexander K. Tagantsev, Igor Stolichnov, Nava Setter, Jeffrey S. Cross, and Mineharu Tsukada. Non-kolmogorov-avrami switching kinetics in ferroelectric thin films. *Phys. Rev. B*, 66:214109, Dec 2002. doi:10.1103/PhysRevB.66.214109. URL https://link.aps.org/doi/10.1103/PhysRevB.66.214109.

[31] Maggie Kingsland, Sergey Lisenkov, and Inna Ponomareva. Unveiling electrocaloric potential of antiferroelectrics with phase competition. *Advanced Theory and Simulations*, 1(11):1800096, 2018. doi:https://doi.org/10.1002/adts.201800096. URL https://onlinelibrary.wiley.com/doi/abs/10.1002/adts.201800096.

[32] Feizhou He and B. O. Wells. Lattice strain in epitaxial $BaTiO_3$ thin films. *Applied Physics Letters*, 88(15):152908, 2006. doi:10.1063/1.2194231. URL https://doi.org/10.1063/1.2194231.

[33] K. J. Choi, M. Biegalski, Y. L. Li, A. Sharan, J. Schubert, R. Uecker, P. Reiche, Y. B. Chen, X. Q. Pan, V. Gopalan, L.-Q. Chen, D. G. Schlom, and C. B. Eom. Enhancement of Ferroelectricity in Strained $BaTiO_3$ Thin Films. *Science*, 306(5698):1005–1009, 2004. doi:10.1126/science.1103218. URL https://www.science.org/doi/abs/10.1126/science.1103218.

[34] Darrell G. Schlom, Long-Qing Chen, Chang-Beom Eom, Karin M Rabe, Stephen K Streiffer, and Jean-Marc Triscone. Strain tuning of ferroelectric thin films. *Annual Review of Materials Research*, 37(1):589–626, 2007. doi:10.1146/annurev.matsci.37.061206.113016. URL https://doi.org/10.1146/annurev.matsci.37.061206.113016.

Hidden variable in the electrocaloric effect of ferroics

Ravi Kashikar[1, §, *], Subhashree Chatterjee[2, §], Folarin Shola Taofeek[1], Abhisikta Barman[2], Shubhankar Barman[3], Sohini Kar-Narayan[4], Anuja Datta[3,4], Sergey Lisenkov[1], Devajyoti Mukherjee[2,*], and Inna Ponomareva[1,*]

[1] Department of Physics, University of South Florida, Tampa, Florida 33620, USA
[2]School of Physical Sciences, Indian Association for the Cultivation of Science, 2A & 2B Raja S. C. Mullick Road, Kolkata 700032, India
[3]School of Applied and Interdisciplinary Sciences, Indian Association for the Cultivation of Science, 2A & 2B Raja S. C. Mullick Road, Kolkata 700032, India
[4]Department of Materials Science & Metallurgy, University of Cambridge, 27 Charles Babbage Road, Cambridge CB3 0FS, United Kingdom
[*]ravik@usf.edu, sspdm@iacs.res.in, iponomar@usf.edu
[§]These authors contributed equally to the work

13th December 2022

Samples growth and characterization

Target and thin film fabrication: A ceramic target of $(Ba_{0.85}Ca_{0.15})(Ti_{0.9}Zr_{0.1})O_3$ was prepared by a conventional solid state reaction starting from high purity (99.99%) powders. The source materials $Ba(CO_3)_2$, $Ca(CO_3)_2$, ZrO_2, and TiO_2 (all from Alfa Aesar) were weighed in a stoichiometric amount, dispersed in isopropanol to form a homogenous solution, dried, and calcined at 1300°C for 5 h. The resulting powder was ball milled for 24 h in hexane and subsequently pressed into pellets. Polyvinyl alcohol was added to the powder to improve the pressing behavior. The pressed pellet was sintered at 1500°C for 3 h.

$(Ba_{0.85}Ca_{0.15})(Ti_{0.9}Zr_{0.1})O_3$ thin film heterostructures using $La_{0.7}Sr_{0.3}MnO_3$ (LSMO) top and bottom electrodes were fabricated on single-crystal $SrTiO_3$ (STO) (100) substrates using a commercial PLD system (Neocera Pioneer 120 Advanced). The optimized growth parameters were similar with those in our previous work [**?**], except that the $(Ba_{0.85}Ca_{0.15})(Ti_{0.9}Zr_{0.1})O_3$ films were deposited under high ambient oxygen pressure P_{O_2} of 1000 mTorr in PLD to minimize oxygen vacancy defect formation during film growth. In the optimized synthesis process, the LSMO and $(Ba_{0.85}Ca_{0.15})(Ti_{0.9}Zr_{0.1})O_3$ targets were sequentially ablated using a KrF excimer laser (Lambda Physik, λ = 248 nm, frequency = 5 Hz, fluence = 4 Jcm^{-2}) inside a deposition chamber equipped with a multi-target carousel that allowed for the in-situ deposition of multilayers with clean interfaces. A distance of 5 cm was maintained between the substrate and the targets during the depositions. Prior to growing the LSMO layer, the STO substrate was annealed inside the PLD chamber at 800°C under a P_{O_2} of 1000 mTorr for 4 hours. An initial layer of LSMO ($\sim$ 50 nm

thickness) was deposited on an STO substrate at 800°C under a background P_{O_2} of 10 mTorr. This initial LSMO layer acted as the bottom electrode during the polarization of the $(Ba_{0.85}Ca_{0.15})(Ti_{0.9}Zr_{0.1})O_3$ thin films. The subsequent $(Ba_{0.85}Ca_{0.15})(Ti_{0.9}Zr_{0.1})O_3$ layer was deposited at 750°C under a high P_{O_2} of 1000 mTorr. A shadow mask was used during the $(Ba_{0.85}Ca_{0.15})(Ti_{0.9}Zr_{0.1})O_3$ layer deposition to preserve an open access to the LSMO bottom electrode. After the $(Ba_{0.85}Ca_{0.15})(Ti_{0.9}Zr_{0.1})O_3$ layer deposition, top LSMO electrodes of 100 μm in diameter and 50 nm thickness were deposited using a shadow mask at 750°C under a P_{O_2} of 10 mTorr. After deposition, the PLD chamber was flooded with pure oxygen (1000 mTorr) and the samples were gradually cooled down to room temperature ($\sim$ 4 h). The thicknesses of the LSMO and $(Ba_{0.85}Ca_{0.15})(Ti_{0.9}Zr_{0.1})O_3$ layers were kept constant at $\sim$ 50 nm and $\sim$ 100 nm, respectively. While several samples were deposited to optimize the growth conditions, here we only present the results from the optimized $(Ba_{0.85}Ca_{0.15})(Ti_{0.9}Zr_{0.1})O_3$ thin film.

Characterization: The crystallinity and phase purity in the bulk and thin films were characterized by x-ray diffraction (XRD) with a Rigaku Smart Lab 9 kW XG diffractometer equipped with a 5-axis goniometer using collimated parallel beam Cu Kα radiation (λ = 1.5406 Å). The chemical composition of the bulk and thin films film were determined using Raman spectroscopy (Nd:YAG Laser Raman spectrophotometer JY Horiba-T6400 equipped with a Synopse CCD camera), energy dispersive spectroscopy (EDS) attached with a scanning electron microscope (SEM, JEOL-JSM-7500F) and X-ray photoelectron spectrometer (XPS, Omicron, model 1712-62-11) using non-monochromatic Al Kα (1486.7 eV) X-ray source operating at 150 W (15 kV and 10 mA). The surface morphology of the bulk and thin films were investigated using scanning electron microscopy (FEI Nova NanoSEM) and atomic force microscope (AFM, Asylum Research MFP-3D). Interfacial microstructure in the $(Ba_{0.85}Ca_{0.15})(Ti_{0.9}Zr_{0.1})O_3$ heterostructure was analysed using high-resolution transmission electron microscopy (HRTEM; FEI Tecnai F 20 S-Twin TEM). A sample for cross-sectional TEM analysis was prepared by surface milling a 5 μm $\times$ 10 μm rectangular strip of 100 nm thickness using a focused ion beam (FIB; JOEL 4500 FIB/SEM) and Pt-welding it to a Cu TEM grid. Electrical measurements of the bulk ceramic were conducted with a planar capacitor structure with using circular ($\sim$ 200 μm in diameter) Au top and bottom electrodes ($\sim$ 100 nm in thickness) that were sputtered through a stainless-steel shadow mask. The real electrode size was measured and calibrated with optical microscope before electrical measurements. Electrical measurements of the fabricated $(Ba_{0.85}Ca_{0.15})(Ti_{0.9}Zr_{0.1})O_3$ thin film capacitor using LSMO top and bottom electrodes were performed using a microprobe station and camera. Measurements of the dielectric constant and loss tangent over a broad frequency and temperature range were conducted by using a precision digital LCR meter (Wayne Kerr 41100) with a perturbation voltage of 1 V. Ferroelectric properties were characterized using a Precision LC II Ferroelectric test system (Radiant Technologies Inc.) with 500V in-built source equipped with a microprobe station. Polarization-electric field (P-E) loops were collected using bipolar triangular voltages waves with a frequency of 1 kHz. For the measurement of temperature-dependent dielectric and polarization properties, the samples were mounted on a heater stage inside an inert sealed bespoke chamber with a heating rate of 2°C min^{-1}.

Epitaxial strain analysis using XRD

From insets (I) and (II) of Extended Data Fig. 3(a), the occurrence of the $(Ba_{0.85}Ca_{0.15})(Ti_{0.9}Zr_{0.1})O_3$ (001) and (111) peaks, respectively, as compared to the corresponding peaks of the bulk $(Ba_{0.85}Ca_{0.15})(Ti_{0.9}Zr_{0.1})O_3$ target (vertical dotted lines); indicate an out-of-plane elongation and an in-plane contraction of the out-of-

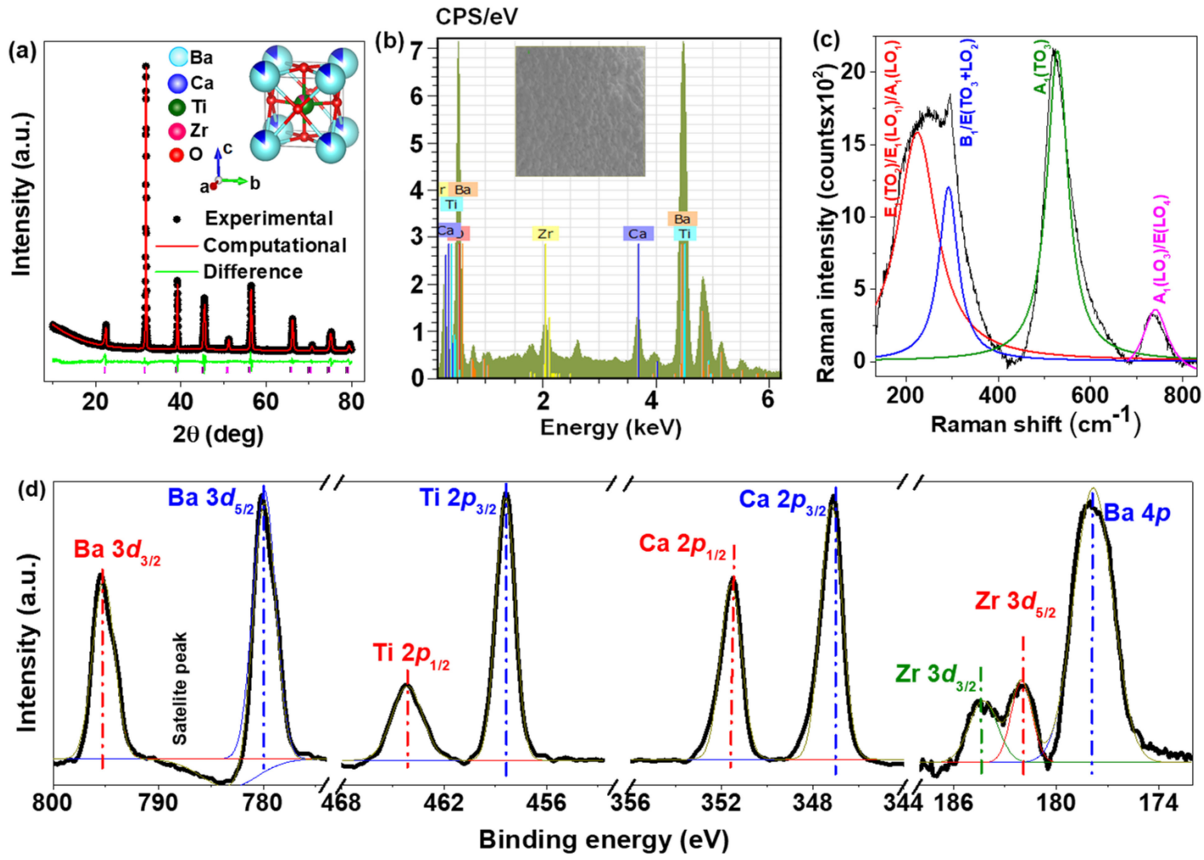

Figure S1: (a) XRD $\theta - 2\theta$ pattern and Rietveld refinement of $(Ba_{0.85}Ca_{0.15})(Ti_{0.9}Zr_{0.1})O_3$ (BCZT) target. The observed peak positions are consistent with the reported JCPDS data (CIF no.1507756). The unit cell lattice parameters calculated from the refinement are c = 4.012 Å and a = b = 4.005 Å. Inset shows the simulated BCZT unit cell structure. (b) EDS spectra and SEM image of the as-prepared bulk target. The stoichiometric composition obtained from EDS measurement was consistent with the nominal composition. i.e., $(Ba_{0.85}Ca_{0.15})(Ti_{0.9}Zr_{0.1})O_3$. (c) Room temperature Raman spectra of BCZT target. (d) XPS spectra of core level Ba 3d, Ti 2p, Ca 2p, and Zr 3d for the as-prepared $(Ba_{0.85}Ca_{0.15})(Ti_{0.9}Zr_{0.1})O_3$ target. The chemical composition as calculated from the XPS analyses $(Ba_{0.85\pm0.01}Ca_{0.15\pm0.01})(Ti_{0.9\pm0.01}Zr_{0.1\pm0.01})O_3$ matches with the nominal composition. The cationic site occupancy ratio (B/A site) for the ABO_3-type $(Ba_{0.85}Ca_{0.15})(Ti_{0.9}Zr_{0.1})O_3$ unit cell as calculated from the XPS spectra was found to be (Ti+Zr/Ba+Ca) = 1.01 which was very close to the ideal ratio of 1 from the BCZT unit cell.

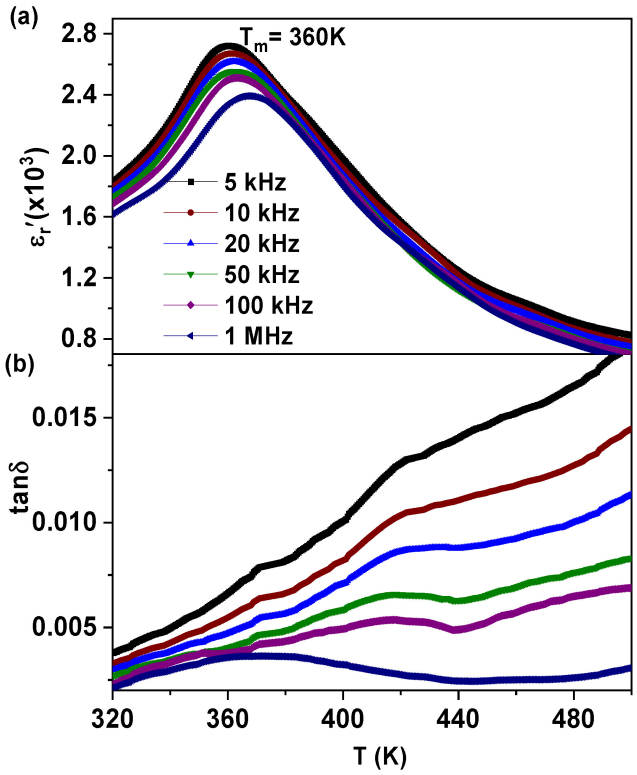

Figure S2: Temperature dependent (a) real part of dielectric constant and (b) tanδ loss at different frequencies from 5 kHz to 1 MHz for $(Ba_{0.85}Ca_{0.15})(Ti_{0.9}Zr_{0.1})O_3$ bulk ceramic. The dielectric maxima temperature, T_m is at 360 K.

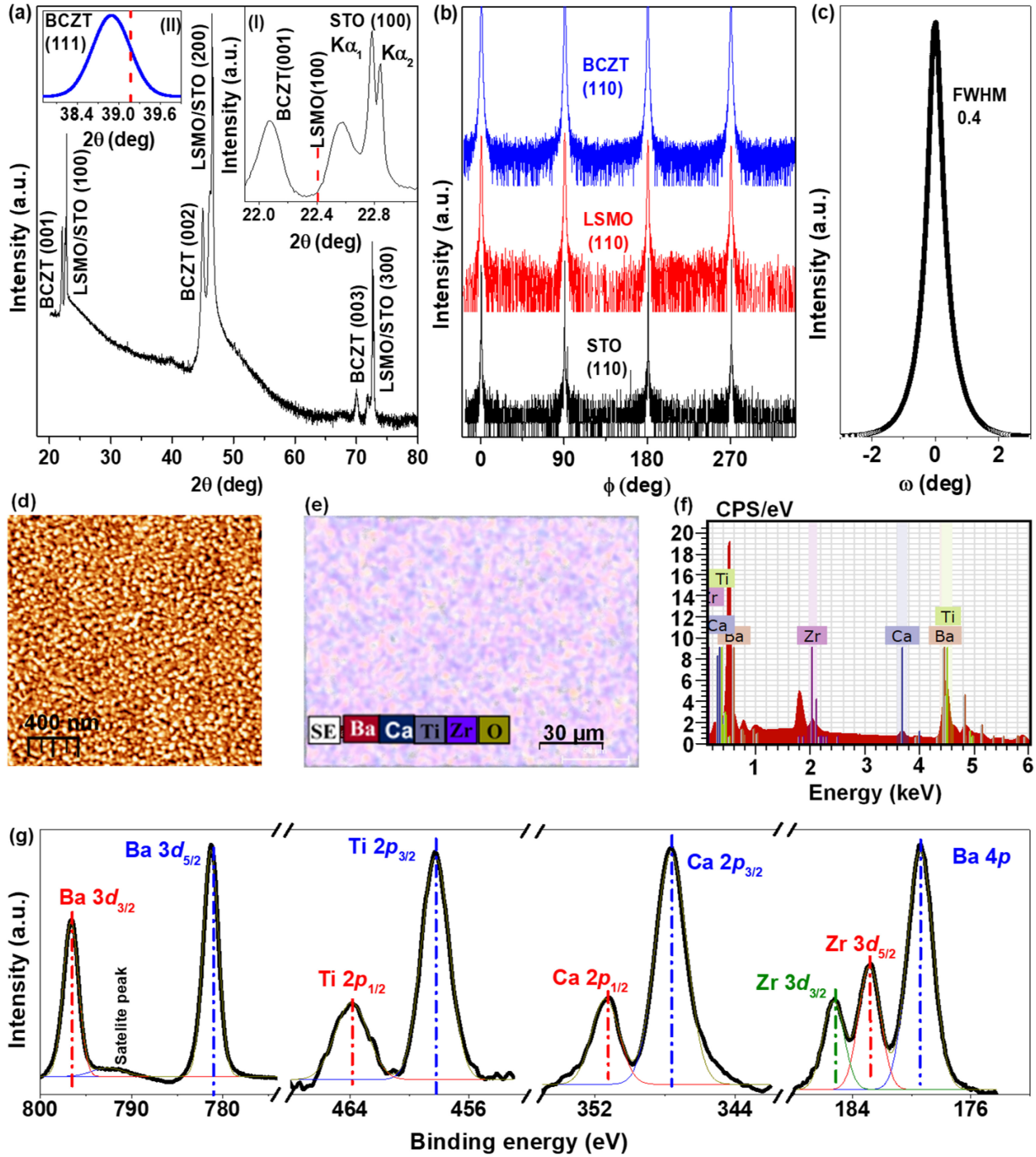
(a)
BCZT (111)
(II)
38.4 39.0 39.6
2θ (deg)
(I)
STO (100)
Kα1
Kα2
BCZT(001)
LSMO(100)
22.0 22.4 22.8
2θ (deg)
Intensity (a.u.)
BCZT (001)
LSMO/STO (100)
BCZT (002)
LSMO/STO (200)
BCZT (003)
LSMO/STO (300)
20 30 40 50 60 70 80
2θ (deg)
(b)
BCZT (110)
LSMO (110)
STO (110)
Intensity (a.u.)
0 90 180 270
ϕ (deg)
(c)
FWHM 0.4
Intensity (a.u.)
-2 0 2
ω (deg)
(d)
400 nm
(e)
SE Ba Ca Ti Zr O
30 μm
(f)
CPS/eV
Ti
Ca
Ba
Zr
Ca
Ti
Ba
Energy (keV)
(g)
Ba 3d5/2
Ba 3d3/2
Satellite peak
Ti 2p3/2
Ti 2p1/2
Ca 2p3/2
Ca 2p1/2
Ba 4p
Zr 3d5/2
Zr 3d3/2
Intensity (a.u.)
800 790 780 464 456 352 344 184 176
Binding energy (eV)

Figure S3: (a) XRD $\theta-2\theta$ pattern of the $(Ba_{0.85}Ca_{0.15})(Ti_{0.9}Zr_{0.1})O_3$/LSMO/STO thin film heterostructure. In all cases, only strong (00l) (l = 1, 2, and 3) diffraction peaks of the tetragonal $(Ba_{0.85}Ca_{0.15})(Ti_{0.9}Zr_{0.1})O_3$ phase are observed along with the (l00) (l = 1, 2, and 3) peaks of the pseudo-cubic perovskite LSMO phase (a = 3.87 Å, JCPDS 01-089-4461) and the single-crystal STO (100) substrate (cubic, a = 3.905 Å), confirming the cube-on-cube epitaxial growth, with no traces of impurity peaks within the resolution limits of the XRD. Due to the close proximity of the $(Ba_{0.85}Ca_{0.15})(Ti_{0.9}Zr_{0.1})O_3$ (001) and the LSMO and STO (100) peaks, a close-up view is shown in the inset (I), where the vertical dotted line marks the position of the $(Ba_{0.85}Ca_{0.15})(Ti_{0.9}Zr_{0.1})O_3$ (001) peak from the bulk XRD data (see Extended Data Fig.S1 (a)). Inset (II) shows an asymmetric XRD $2\theta-\omega$ scan performed about the $(Ba_{0.85}Ca_{0.15})(Ti_{0.9}Zr_{0.1})O_3$ (111) crystallographic plane for the thin film heterostructure. (b) Representative XRD azimuthal (ϕ) scans performed about the $(Ba_{0.85}Ca_{0.15})(Ti_{0.9}Zr_{0.1})O_3$ (BCZT) (110), LSMO (110), and STO (110) crystallographic planes for the heterostructure. The repeated occurrence of sharp peaks at regular intervals of 90° confirms the 4-fold symmetry of the individual layers and cube-on-cube epitaxial growth of the heterostructure. (c) XRD rocking curve performed about the (001) plane showing narrow full-width-half-maxima (FWHM) of 0.4° for the heterostructure confirming the excellent in-plane orientation in the thin film. (d) Topographic AFM image of the top $(Ba_{0.85}Ca_{0.15})(Ti_{0.9}Zr_{0.1})O_3$ layer in the heterostructure which exhibits smooth particulate-free surface morphology with low roughness (Rrms $\sim$ 0.6 nm) and uniform grain sizes (about 40 nm), implying a good uniform and homogeneous growth. (e) EDS elemental hypermap of the $(Ba_{0.85}Ca_{0.15})(Ti_{0.9}Zr_{0.1})O_3$ surface indicating its uniform stoichiometric growth. (f) EDS spectra and (g) XPS spectra of constituent elements of the $(Ba_{0.85}Ca_{0.15})(Ti_{0.9}Zr_{0.1})O_3$ thin film. The chemical composition of the layer as calculated from the XPS analyses is $(Ba_{0.85\pm0.02}Ca_{0.15\pm0.02})(Ti_{0.9\pm0.01}Zr_{0.1\pm0.01})O_3$ which matches with the nominal composition of $(Ba_{0.85}Ca_{0.15})(Ti_{0.9}Zr_{0.1})O_3$ target. The cationic site occupancy ratio (B/A site) for the ABO_3-type $(Ba_{0.85}Ca_{0.15})(Ti_{0.9}Zr_{0.1})O_3$ unit cell as calculated from the XPS spectra was found to be (Ti+Zr/Ba+Ca) = 0.99 which was very close to the ideal ratio of 1 from the $(Ba_{0.85}Ca_{0.15})(Ti_{0.9}Zr_{0.1})O_3$ unit cell.

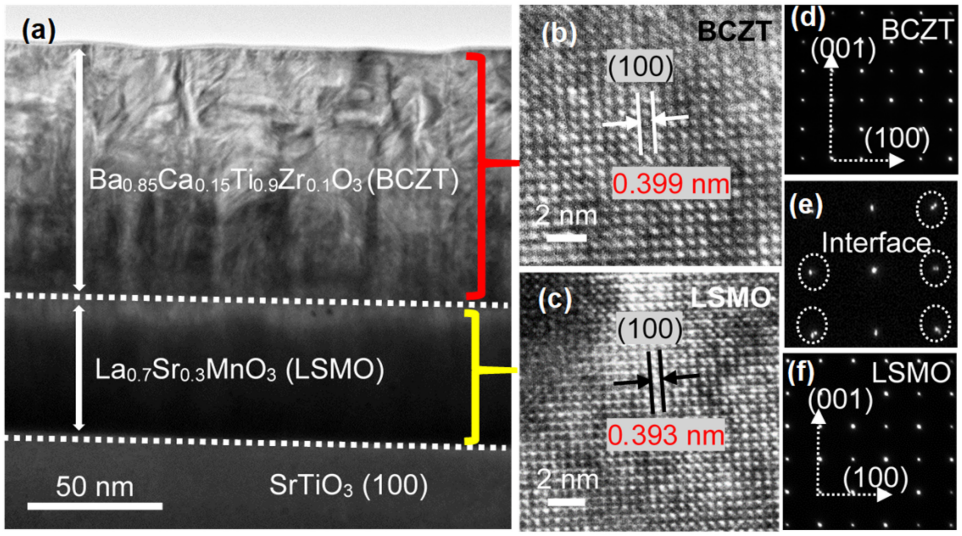

Figure S4: (a) Cross-sectional TEM image of $(Ba_{0.85}Ca_{0.15})(Ti_{0.9}Zr_{0.1})O_3$/LSMO heterostructure grown on $SrTiO_3$ (100) substrate revealing sharp and flat interfaces between the layers. (b, c) HRTEM images of the BCZT and LSMO layers captured from the regions marked with red and yellow brackets in (a), respectively. The measured d-spacing values for $(Ba_{0.85}Ca_{0.15})(Ti_{0.9}Zr_{0.1})O_3$ (d_{100} = 0.399 nm) and LSMO (d_{100} = 0.393 nm) in Extended Data Figs. S4 (b) and (c) are consistent with those obtained from the XRD analyses. (d, e, f) Linear dotted single-crystalline SAED patterns captured from the BCZT layer, near the BCZT-LSMO interface and the LSMO layer of BCZT/LSMO heterostructure, respectively. The directions of the (001) and (100) planes are marked with white arrows in (d, e, f). The SAED pattern near the BCZT-LSMO interface shows double dots from adjacent planes [marked by dotted circles in Extended Data Fig. S4 (e)] between the BCZT and the LSMO layers

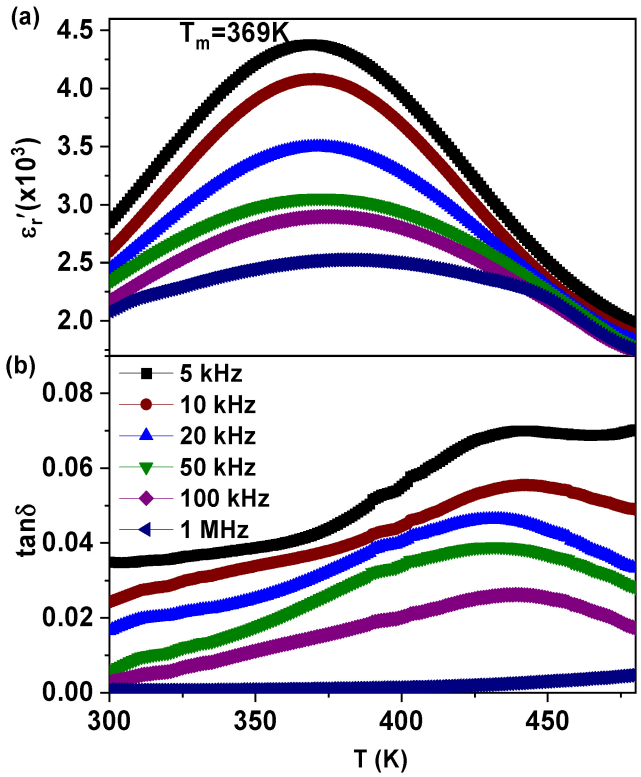

Figure S5: Temperature dependent (a) real part of dielectric constant and (b) tanδ loss at different frequencies for $(Ba_{0.85}Ca_{0.15})(Ti_{0.9}Zr_{0.1})O_3$ thin film heterostructure. The low values of the dielectric loss (tanδ 0.07) measured within the same temperature and frequency ranges indicate the negligible leakage in the BCZT/LSMO thin film capacitor. The dielectric maxima, T_m for the thin film (T_m= 369 K) is slightly higher than that of the bulk BCZT target (T_m = 360 K) at the same frequency.

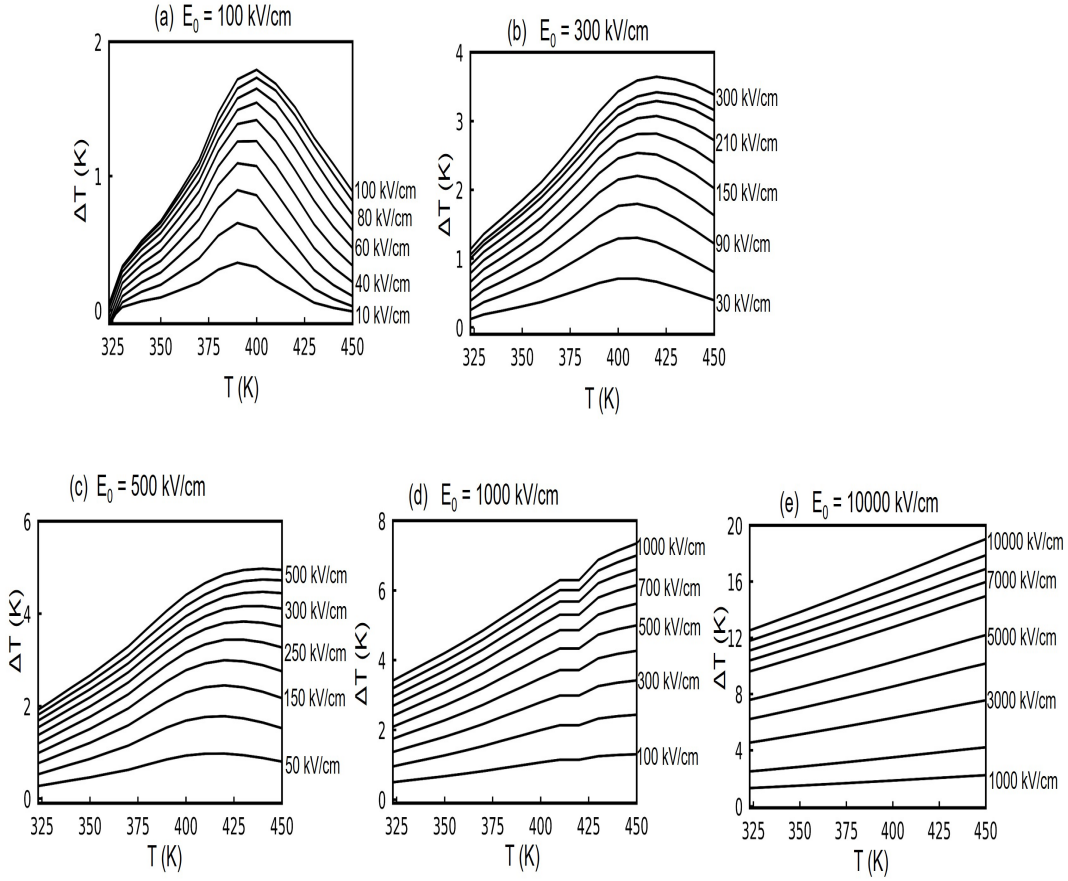

Figure S6: Hysteresis loops for BCZT thin film measured in different ranges of electric field: [-400:400] kV/cm (a), [-600:600] kV/cm (b), [-750:750] kV/cm (c); the associated dependencies of the polarization on temperature for different electric fields and for E_0 as indicated in the titles (b), (e) and (h); the associated electrocaloric change in temperature as a function of temperature obtained from the indirect approach for E_0 as indicated in the titles (c), (f) and (i)

plane (a_{per}) and in-plane lattice parameters (a_{par}), respectively, in the $(Ba_{0.85}Ca_{0.15})(Ti_{0.9}Zr_{0.1})O_3$ layer as compared to the bulk $(Ba_{0.85}Ca_{0.15})(Ti_{0.9}Zr_{0.1})O_3$ target. In this case, the bulk $(Ba_{0.85}Ca_{0.15})(Ti_{0.9}Zr_{0.1})O_3$ unit cell (tetragonal, a = b = 4.005 Å, c = 4.012 Å, see Extended Data Fig. 1(a) experiences an in-plane compressive strain (i.e. out-of-plane tensile strain) in order to match the slightly smaller lattice parameter of the underlying LSMO layer (a = 3.935 Å) in the epitaxial heterostructure [**?**, **?**]. The calculated values of the lattice parameters from the XRD symmetric and asymmetric scans shown in Extended Data Fig. 3(a) are a_{per} = 4.024(4) Å and a_{par} = 3.999 (6) Å which gives a large out-of-plane tensile strain ϵ_{per} = (a_{per} - c)/c $\simeq$ 0.29% and correspondingly a significant in-plane compressive strain ϵ_{par} = (a_{par} - a)/a $\simeq -0.15\%$ in the $(Ba_{0.85}Ca_{0.15})(Ti_{0.9}Zr_{0.1})O_3$ layer in the heterostructure. This results in higher out-of-plane tetragonal distortion (i.e. $a_{per}/a_{par} - 1$) of $\sim 0.62\%$ in the $(Ba_{0.85}Ca_{0.15})(Ti_{0.9}Zr_{0.1})O_3$ unit cell in the film as compared to the bulk $(Ba_{0.85}Ca_{0.15})(Ti_{0.9}Zr_{0.1})O_3$ unit cell (c/a – 1 = 0.17%).

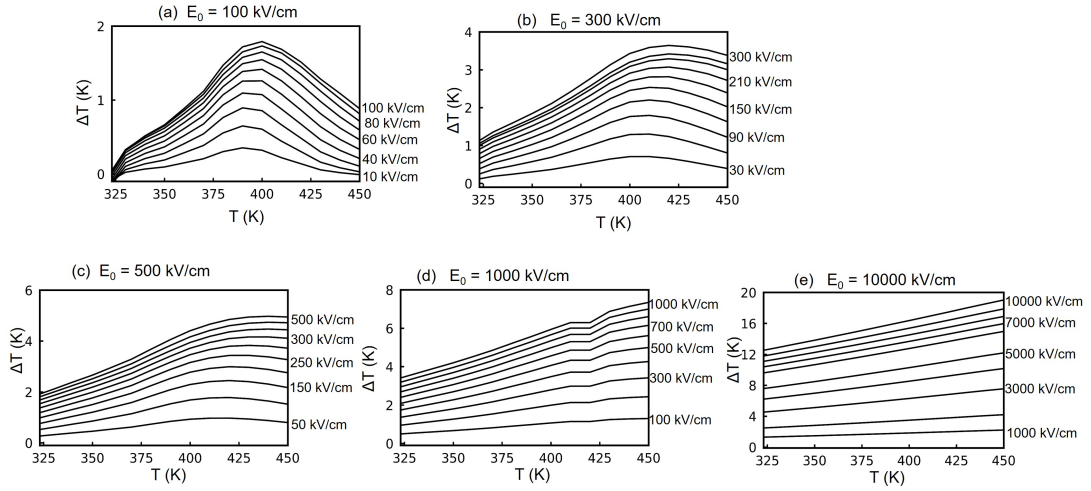

Figure S7: Electrocaloric change in the temperature as a function of temperature for E_0 =100 kV/cm for various tensile strains (as indicated in the titles) computed from indirect approach applied on MD simulation data.

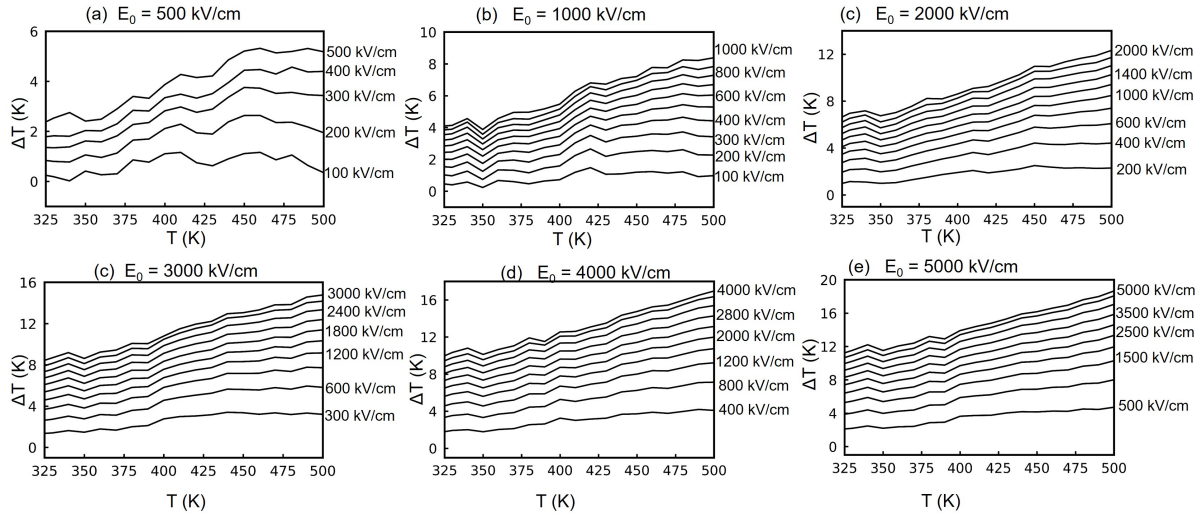

Figure S8: Ferroelectric hysteresis loops obtained in isothermal MD computations for $BaTiO_3$ for the electric fields :[-50:50] kV/cm (a), [-500:500] kV/cm (b) ; and [-5000:5000] kV/cm (c). Dependence of polarization on temperatures (d)-(f) obtained from the data of panels (a)-(c), respectively. Electrocaloric change in temperature (g)-(h) computed from dependencies of panels (d)-(f) using Eq. (1).